KRONOS FUSION ENERGY

PAPER 2.13 · THE KRONOS 2026 SERIES

Toroidal Rotation, Flow-Shear Stabilization and Error-Field Correction in a Compact Spherical-Tokamak Breeder: Residual Transport and Locked-Mode Avoidance

A negative-triangularity spherical-tokamak breeder that operates near its no-wall stability limit is not held there passively: toroidal rotation, sheared flow and the correction…

Read it live — 3-D model · physics validator · film series

BY P I FORD AND G L KULCINSKI

2026 · EDITORIAL EDITION

THE OFFICIAL RECORD

What this document is, and how to read its numbers

This is a combined editorial. It gathers, in one volume, the two design studies Kronos Fusion Energy released in 2026 — a compact spherical-tokamak tritium/helium-3 breeder and a deuterium–helium-3 tandem-mirror generator — together with the intellectual-property estate, the people, and, in the internal edition, the full commercial case. The scientific text is the same text that appears in the arXiv preprints and the journal submissions; the editorial adds the apparatus a reader needs to hold the whole program at once, and nothing in the physics is altered to fit it.

THE HONESTY STANCE IS THE ASSET

Every headline quantity carries an **evidence class** — DERIVED RECOMPUTED MEASURED REQUIREMENT — and, where a number is a modelled extrapolation rather than a demonstrated value, it is labelled as such and its downside is shown next to it. Several quantities in the underlying corpus moved after first publication; where a value has been withdrawn or restated, the record says so plainly. This is deliberate: a diligence team will find the load-bearing assumptions, so the document surfaces them first.

TWO EDITIONS

This volume is issued in two editions. The **public edition** (light) carries the physics and the design only — no dollar, price, or per-kilogram figure appears anywhere in it. The **internal edition** (dark) adds the economics, the funding architecture, and the defense-commercial analysis, and is marked *Confidential* accordingly; it is not for public distribution. Where the commercial case rests on a modelled assumption rather than a demonstrated one, it is labelled as such and its downside is shown alongside it, on the same terms as the physics.

TITLE	The Kronos Fleet — Hyperion · Aegis · MetroVolt: A Combined Design & Commercialization Study
AUTHOR	Priyanca Ford, Founder & CEO, on behalf of Kronos Fusion Energy
EDITION	2026 Combined Editorial · first issue
COMPANION WORKS	The five-paper arXiv drop — (1) Breeder, (2) Burner, (3) REBCO magnet & tape, (4) Direct Energy Conversion, (5) AI/ML/Quantum control — with matching numbered Zenodo deposits, plus the IOP journal and IAEA-FEC submissions. Patents were filed before the drop.
NAMING	Hyperion = the breeder; Aegis (defense) and MetroVolt (data-center) = one generator in two housings. Internal mode letters (D1, L) do not appear on public surfaces.
STATUS	Conceptual design & simulation study. Nothing herein is a construction commitment.

HOW TO READ THIS VOLUME

The fleet at a glance, and the way its numbers are marked

This volume opens with *Orientation*, presents the five research papers as a bound sequence, and closes with the *Apparatus*. *Foundations* sets out the three general results both machines rest on. *Paper One* is the Hyperion breeder; *Paper Two* the Aegis / MetroVolt generator; *Papers Three, Four and Five* are the enabling science — high-field REBCO magnets and tape, direct energy conversion, and the AI / ML / quantum control stack. A *Digital Twin & 3-D Model* part follows, then the *Environmental* profile. The *Economics* and levelized cost and the *Business Case* and diligence record appear in the internal edition only; the *Simulations* proof record and the Apparatus — patent portfolio, team, limitations, and sources — close both editions.

THE FLEET AT A GLANCE

	HYPERION	AEGIS	METROVOLT
Role	Strategic-isotope foundry	Defense installation power	Campus power
Machine	**Spherical tokamak**	**Tandem mirror**	**Tandem mirror**
Fuel	Deuterium–tritium	Deuterium–helium-3	Deuterium–helium-3
Delivers	Tritium · ^{3}He · 14 MeV n	Resilient installation power	Firm campus power
Physics bar	**Fusion gain only**	Closure (gates named)	Closure + lunar ^{3}He
In the fleet	Breeds the fuel	Proves the generator	Commercial destination

HOW THE NUMBERS ARE MARKED

Every headline quantity carries an evidence class — DERIVED from first principles, RECOMPUTED from raw data, MEASURED in hardware, or a REQUIREMENT yet to be met. Financial figures carry a case label and are confined to the internal (confidential) edition. Values that moved after first publication are shown as withdrawn or restated rather than quietly changed. A capability you can evaluate is one whose limits are on the page.

ABSTRACT

Toroidal Rotation, Flow-Shear Stabilization and Error-Field Correction in a Compact Spherical-Tokamak Breeder: Residual Transport and Locked-Mode Avoidance

A negative-triangularity spherical-tokamak breeder that operates near its no-wall stability limit is not held there passively: toroidal rotation, sheared $E \times B$ flow and the correction of residual error fields are the active layer that keeps a quiet core quiet and keeps a rotating plasma from braking into a locked mode. We formulate this layer from first principles for the Kronos Hyperion breeder at its frozen design point ($I_p = 9.66$ MA, $\delta = -0.30$, $B_0 = 8$ T, $\kappa = 2.0$, $R_0 = 1.20$ m, $Q = 3.076$, $P_{\text{fus}} = 85.04$ MW). The governing model couples flux-surface-averaged toroidal angular-momentum transport, the radial-force-balance radial electric field and its Hahm–Burrell shearing rate, the drift-kinetic bootstrap current, the resistive-wall-mode dispersion relation, and the Fitzpatrick error-field torque balance; the numerical formulation ties them to a free-boundary Grad–Shafranov equilibrium and a spectral drift-kinetic solve executed on the NVIDIA GPU HPC campaign. From the reconstruction we find every confinement-region surface outside the $q = 1$ radius ($\psi_N \gtrsim 0.72$) is Mercier-stable with a margin growing from $+0.23$ to $+47$ toward the edge, and infinite-n ballooning-stable in first stability at $\alpha_{\max} \approx 0.55$. The binding constraint is the global $n = 1$ external kink: the normalized beta $\beta_N = 2.13$ sits below the no-wall Troyon limit with a $1.31\times$ margin ($1.64\times$ to the ideal wall). A full linearized-Fokker–Planck NEO calculation gives a parallel bootstrap current 0.81–$0.87\times$ the Sauter value across $r/a = 0.5$–0.7 in the banana regime ($\nu_e^* \approx 0.012$), removing a systematic $\sim 17\,\%$ over-prediction from the current profile the controller shapes. High operating density raises the $2/1$ locked-mode penetration threshold to $b_{\text{th}} \approx 9.8 \times 10^{-4}$; at ≤ 1 mm coil assembly the intrinsic resonant field stays a factor 2.3 below it, so the breeder is intrinsically error-field tolerant and can run without resonant-magnetic-perturbation coils. On this base we specify a flow-shear/rotation controller, a tearing/locked-mode detector with electron-cyclotron current drive, and a vertical-stability PD controller (open-loop $\gamma\tau_w = 8.05$, arrested in 3.5 ms), each with pre-set acceptance criteria, delivering the residual-transport and locked-mode-avoidance layer for autonomous operation.

Open-access deposit (code & data, CC BY 4.0): DOI 10.5281/zenodo.22645907 · Zenodo community *kronos_fusion_energy*. Explore it live: interactive 3-D model · physics validator.

Keywords: toroidal rotation · flow-shear stabilization · error-field correction · resistive-wall mode · locked mode · neoclassical bootstrap · negative triangularity · spherical tokamak

CONTENTS

Table of Contents

NOMENCLATURE

Symbols, units, and the names of things

Q	plasma (fusion) gain, P_{fus}/P_{aux}
Q_E	engineering gain, net electric out / recirculating in
H_{98}	confinement enhancement over the IPB98(y,2) scaling
Z_{eff}	effective ion charge
c_{ee}	electron–electron bremsstrahlung leading coefficient, 2.120022 (exact)
τ_E	energy confinement time
I_p	plasma current
R_0, a	major radius, minor radius
κ, δ	elongation, triangularity
β_N	normalized plasma beta (Troyon-normalized)
TBR	tritium breeding ratio
DEC	direct energy conversion
CF	plant capacity factor (availability)
FOAK / NOAK / BOAK	first / n^{th} / best of a kind
Hyperion	the ST breeder (internal: Mode D2)
Aegis	the generator, defense/installation housing (internal: Mode M)
MetroVolt	the generator, data-center housing (Mode M)

§ 1

Introduction

The Kronos Hyperion breeder is a compact, high-field spherical tokamak built around a negative-triangularity ($\delta = -0.30$) plasma whose core is quiet by construction. At $B_0 = 8$ T, $\kappa = 2.0$ and $R_0 = 1.20$ m behind a 16.84 T centrepost it holds $I_p = 9.66$ MA at $Q = 3.076$ and $P_{\text{fus}} = 85.04$ MW, and nonlinear gyrokinetics confirm that the negative-triangularity shape suppresses ion- and electron-scale turbulence at the operating point. That quiescence is the machine's central advantage, and it is not a passive property. A plasma held near a stability boundary is held there *actively*, and the quantities that hold it are the plasma's rotation, the shear in its $E \times B$ flow, and the correction of the residual non-axisymmetric fields that would otherwise brake that rotation.

Three physical facts organize the problem. First, rotation and conducting-wall coupling stabilize the $n = 1$ resistive-wall mode (RWM) when a plasma runs near the no-wall external-kink boundary [1,2]. Second, sheared $E \times B$ flow suppresses the drift-wave turbulence that otherwise sets the transport, quenching fluctuations when the shearing rate exceeds the maximum linear growth rate [3,4,5,6]. Third, a static error field resonant with the $q = 2$ surface exerts an electromagnetic braking torque; if it overcomes the viscous restoring torque the rotation collapses at that surface, the field penetrates, and a locked island grows — and a locked mode is the dominant deterministic path to disruption [7,8,9]. These three are coupled: the rotation that stabilizes the RWM is the same rotation that screens the error field, and the flow shear that suppresses turbulence is set by the same radial electric field that the rotation carries.

Prior art. The stabilization of external kink modes by resistive walls and rotation was established theoretically by Bondeson and Ward [1] and demonstrated across DIII-D, NSTX and JT-60U; reviews are given in the ITER Physics Basis MHD chapter [15]. The role of $E \times B$ shear in turbulence suppression traces to Biglari, Diamond and Terry [3], was generalized to shaped finite-aspect-ratio geometry by Hahm and Burrell [4], and is reviewed alongside zonal-flow physics by Burrell [5]. Error-field penetration and the locked-mode bifurcation were placed on a torque-balance footing by Fitzpatrick [7] and calibrated against JET, COMPASS-D and DIII-D by Buttery *et al.* [8]. The neoclassical bootstrap current that anchors the intrinsic rotation and current profile is described analytically by Sauter, Angioni and Lin-Liu [11] and by the drift-kinetic solver NEO [12,13]. Intrinsic (torque-free) toroidal rotation, the regime a low-external-momentum reactor must exploit, is characterized across machines by Rice *et al.* [10]. What has not been assembled — and what this paper provides — is a single, internally consistent treatment of rotation, flow shear and error-field correction anchored to one frozen, reconstructed operating point of a specific negative-triangularity spherical-tokamak breeder, with the stability base solved, the rotation taken from first principles rather than a fit, and each control element carrying a falsifiable acceptance test.

Contribution. We (i) reconstruct the design-point equilibrium free-boundary and locate the single binding ideal-MHD constraint; (ii) derive the coupled governing equations for toroidal momentum transport, the $E \times B$ shearing rate, the bootstrap current, the RWM dispersion relation and the error-field torque balance, and give their numerical formulation; (iii) anchor the rotation and current profile in a full linearized-Fokker–Planck drift-kinetic calculation, reproducing the register's "$\sim 83\%$ of Sauter" figure as real banana-regime physics; (iv) quantify the intrinsic $2/1$ error-field tolerance and show the machine can run without resonant-magnetic-perturbation (RMP) coils; and (v) specify the flow-shear, locked-mode and vertical-stability controllers with pre-set acceptance criteria. This work sits in the Kronos design series alongside the free-boundary equilibrium and ideal-MHD stability study [31], the nonlinear-gyrokinetic negative-triangularity turbulence result [32], the neoclassical-transport and poloidal-flow baseline [33], the disruption, runaway and shattered-pellet study [34], the vertical-stability analysis [35], the bootstrap-aligned steady-state current-drive study [36], and the real-time breeder control suite [37]; the numbers used here are frozen entries of the Kronos Physics De-Risking Register [30].

§ 2

Governing equations and the formal problem

We work in flux coordinates (ψ, θ, ϕ) with ψ the poloidal flux, $B = I(\psi)\nabla\phi + \nabla\phi \times \nabla\psi$, $I = RB_\phi$, and flux-surface average $\langle\cdot\rangle = \oint(\cdot)\,\mathrm{d}\ell/B_p / \oint \mathrm{d}\ell/B_p$. The volume element is $V'(\psi) = \oint \mathrm{d}\ell/(|\nabla\psi|B_p)\cdot 2\pi$. Normalized poloidal flux is $\psi_N = (\psi - \psi_{\text{axis}})/(\psi_{\text{bnd}} - \psi_{\text{axis}})$.

TOROIDAL ANGULAR-MOMENTUM TRANSPORT

The flux-surface-averaged toroidal angular momentum density is $L_\phi = m_i \langle n_i R^2\rangle\,\Omega(\psi)$, with $\Omega = E_r/(RB_\theta) + \ldots$ the toroidal rotation frequency. Conservation of toroidal angular momentum reads

$$\frac{\partial}{\partial t}\big(m_i\langle n_i R^2\rangle\,\Omega\big) + \frac{1}{V'}\frac{\partial}{\partial\psi}\big(V'\,\Pi_{\psi\phi}\big) = \langle R \qquad T\cdot\nabla\phi\rangle \equiv S_\phi,$$

where $\Pi_{\psi\phi}$ is the radial flux of toroidal momentum and S_ϕ the net torque density. The momentum flux decomposes into diffusive, pinch and residual (intrinsic) pieces,

$$\Pi_{\psi\phi} = -\,m_i n_i \langle R^2\rangle\,\chi_\phi\,\frac{\partial\Omega}{\partial\psi} \;+\; m_i n_i \langle R^2\rangle\,V_{\mathrm{p}}\,\Omega \;+\; \Pi^{\text{res}}_{\psi\phi},$$

with momentum diffusivity χ_ϕ tied to the ion heat diffusivity through a turbulent Prandtl number $\mathrm{Pr} = \chi_\phi/\chi_i = \mathcal{O}(1)$, an inward pinch V_{p}, and a residual stress Π^{res} that survives at $\nabla\Omega \to 0$. Because a breeder minimizes external momentum injection, the steady rotation is set by the balance of Π^{res}, the pinch, and the neoclassical toroidal-viscosity (NTV) torque discussed below; equation (1) is the transport equation the flow-shear controller must respect, and Π^{res} is why intrinsic rotation [10] is available at all.

A non-axisymmetric field $\delta \quad B$ breaks toroidal symmetry and exerts an NTV torque that relaxes Ω toward a neoclassical offset:

$$S^{\text{NTV}}_\phi = -\,\mu_{\text{NTV}}(\nu_i, \delta B)\,\big[\Omega - \Omega_{\text{NC}}\big], \qquad \mu_{\text{NTV}} \propto \left(\frac{\delta B}{B}\right)^2, \quad \Omega_{\text{NC}} = -\,\frac{k_{\text{NTV}}}{Z_i e}\frac{\partial T_i}{\partial\psi},$$

so residual error fields enter the momentum balance quadratically in $\delta B/B$. Equation (3) is the mechanism by which an uncorrected error field brakes the plasma; keeping $\delta B/B$ small is therefore a rotation-preservation requirement, not only a mode-stability one.

RADIAL FORCE BALANCE AND THE $E \times B$

ExB shearing rate The radial electric field follows from the ion radial force balance,

$$E_r = \frac{1}{Z_i e\, n_i}\frac{\partial p_i}{\partial r} - v_{\theta,i}B_\phi + v_{\phi,i}B_\theta,$$

with the diamagnetic term dominant at the pressure gradients of the confinement region. The $E \times B$ angular rotation is $\omega_E = E_r/(RB_\theta)$, and the flow shear that acts on turbulence is the Hahm–Burrell shearing rate [4],

$$\gamma_E = \left|\frac{(RB_\theta)^2}{B}\frac{\partial}{\partial\psi}\left(\frac{E_r}{RB_\theta}\right)\right| \;\simeq\; \left|\frac{\partial}{\partial r}\left(\frac{E_r}{B}\right)\right|.$$

The suppression criterion, verified experimentally and in gyrokinetics [3,5,6], is that turbulence is quenched where the shearing rate exceeds the maximum linear growth rate over the unstable spectrum,

$$\boxed{\gamma_E \gtrsim \gamma^{\text{lin}}_{\max} \equiv \max_{k_y}\,\gamma_{\text{lin}}(k_y)}$$

Equation (6) is the quantitative target of the flow-shear controller: it must hold γ_E above the marginal growth rate reported by the companion nonlinear-gyrokinetic study [32] across the confinement region. Negative triangularity lowers $\gamma^{\text{lin}}_{\max}$ (the quiet basin), so the criterion is easier to satisfy at $\delta = -0.30$ than at positive triangularity — the shape and the flow work in the same direction.

NEOCLASSICAL BOOTSTRAP CURRENT AND THE DRIFT-KINETIC EQUATION

The rotation and current profile that the controller shapes are set neoclassically. Writing the distribution as $f_a = f_{a0}(1 + e_a\phi/T_a) + g_a$ with f_{a0} a Maxwellian, the first-order drift-kinetic equation for g_a is

$$v_\parallel \quad b\cdot\nabla g_a - C_a[g_a] = - \quad v_{d,a}\cdot\nabla\psi \,\frac{\partial f_{a0}}{\partial\psi} - \frac{e_a}{T_a} f_{a0}\, v_\parallel \langle E_\parallel B\rangle/\langle B^2\rangle \cdot B,$$

where $v_{d,a}$ is the magnetic drift and C_a the linearized Fokker–Planck collision operator. The parallel bootstrap current is the velocity moment $\langle j_\parallel B\rangle = \sum_a e_a \langle B \int v_\parallel g_a \,\mathrm{d}^3v\rangle$. The analytic Sauter closure [11] parametrizes it as

$$\langle j_\parallel B\rangle_{\rm bs} = -\,I(\psi)\,p_e\left[\mathcal{L}_{31}\frac{\partial \ln p}{\partial\psi} + \mathcal{L}_{32}\frac{\partial \ln T_e}{\partial\psi} + \mathcal{L}_{34}\,\alpha_c\,\frac{p_i}{p_e}\frac{\partial \ln T_i}{\partial\psi}\right],$$

with coefficients $\mathcal{L}_{3k}(f_t, \nu_e^*)$ functions of the trapped fraction f_t and electron collisionality ν_e^*. In the banana regime $\nu_e^* \ll 1$ the Sauter fit is known to over-predict; solving equation (7) directly with a full Fokker–Planck operator (the NEO code [12,13]) yields the reduction quantified in §4.2. The self-consistent bootstrap fraction $f_{\rm bs} = \langle j_\parallel B\rangle_{\rm bs}/\langle j_\parallel B\rangle$ sets the intrinsic current the equilibrium carries and, through equation (4), the diamagnetic E_r that seeds the flow shear.

RESISTIVE-WALL-MODE STABILIZATION BY ROTATION

Whether the near-limit operating point requires active RWM stabilization is set by the external-kink dispersion relation with a resistive wall. For the $n=1$ mode, writing $\hat\beta \equiv \beta_N$ and the no-wall and ideal-wall marginal values $\beta_N^{\rm nw}$ and $\beta_N^{\rm iw}$, the thin-wall dispersion relation in the inertia-free limit is [1,2]

$$\gamma\,\tau_w \;=\; \frac{\hat\beta - \beta_N^{\rm nw}}{\beta_N^{\rm iw} - \hat\beta}\;,$$

so the RWM is unstable ($\gamma > 0$) only in the band $\beta_N^{\rm nw} < \hat\beta < \beta_N^{\rm iw}$. Plasma rotation Ω coupled to dissipation (sound-wave and ion-Landau damping) adds a stabilizing imaginary contribution and removes the mode when Ω exceeds a critical fraction of the Alfv\'en frequency, $\Omega_{\rm crit} \sim (10^{-2}\text{–}10^{-1})\,\omega_A$ [1]. At the Hyperion design point $\hat\beta = \beta_N = 2.13$ lies *below* $\beta_N^{\rm nw} \approx 2.8$, so equation (9) gives $\gamma < 0$: the external kink is stable without a wall, and rotational RWM stabilization is not required at the nominal point. But the no-wall margin is only $1.31\times$; equation (9) shows that a beta excursion of that size enters the RWM band, which is exactly where rotation and wall coupling carry the load. The design point therefore treats rotation not as a nominal necessity but as the cushion for excursions.

ERROR-FIELD PENETRATION AND THE LOCKED-MODE TORQUE BALANCE

The deterministic disruption path is error-field penetration at the $q = 2$ surface. Let Ω_s be the plasma rotation at that surface and b_r the resonant radial field normalized to B_T. The rotation obeys a torque balance between the viscous restoring torque and the electromagnetic (reconnection) torque from the induced island [7]:

$$I_s\,\frac{\mathrm{d}\Omega_s}{\mathrm{d}t} = \underbrace{-\,\mu_s(\Omega_s - \Omega_{s,0})}_{\text{viscous}} \;+\; \underbrace{T_{\rm EM}\,\frac{(b_r/b_c)^2}{1 + (\Omega_s\tau_r)^2}}_{\text{electromagnetic braking}},$$

with τ_r the resistive reconnection time and b_c a normalizing field. Equation (10) is bistable: below a critical amplitude $b_r < b_{\rm th}$ the "unreconnected" branch (fast rotation, screened field) is the only stable root; above $b_{\rm th}$ the rotation collapses discontinuously to the "fully reconnected" branch and a locked island grows. The critical amplitude scales with density and field; the multi-machine empirical calibration [8] gives

$$\frac{b_{\rm th}}{B_T} \;\propto\; n_e^{0.6}\,B_T^{0.5}\,R^{\gamma_R},$$

so a compact high-density device has a *raised* penetration threshold and is intrinsically error-field tolerant. The intrinsic resonant field is a tolerance-stack quantity: a coil-set positioning error δr couples to the $2/1$ harmonic as $b_r \simeq k\,(\delta r/R_0)$ with $k \sim 0.5$. Sections 4.4 quantifies both sides of the inequality $b_r < b_{\rm th}$.

VERTICAL STABILITY AS A ROTATION-INDEPENDENT CONSTRAINT

Elongation $\kappa = 2.0$ makes the axisymmetric ($n = 0$) vertical mode unstable; unlike the modes above, it is independent of rotation and is held by a resistive wall plus feedback. In the massless rigid-shift model the wall-slowed growth rate is $\gamma_z = (n_s - 1)/[\tau_w(1 - n_s + \Delta)]$, conventionally quoted through the stability index $\gamma_z\tau_w$. A proportional-derivative controller of coil-field gains (K_p, K_d) acting on the vertical displacement ξ_z closes the loop with characteristic polynomial

$$\tau_w\, s^2 + \big(K_d - \gamma_z\tau_w + 1\big)s + \big(K_p - \gamma_z\big) = 0,$$

which is Hurwitz-stable (both closed-loop poles in the left half-plane) for $K_p > \gamma_z$ and $K_d > \gamma_z\tau_w - 1$. Equation (12) sets the gain thresholds and the converter authority reported in §4.5; it is the third leg of the locked-mode-avoidance layer because a vertical-displacement event that is not arrested itself terminates in a disruption.

§ 3

Computational methodology: the NVIDIA GPU HPC campaign

All equilibrium, drift-kinetic, gyrokinetic and extended-MHD calculations underlying this paper were produced on the Kronos NVIDIA GPU HPC campaign — an owned, air-gappable estate of NVIDIA A100/H100 accelerators (Lambda fleet, with A10 nodes for pre/post-processing) and an in-house verification node — together with reduced-metric analyses on a local CPU node. The campaign runs the standard open reference codes rather than bespoke solvers, so every number is reproducible against a published tool. We name the codes actually executed for this study and their problem scale; no compute cost is reported.

FREE-BOUNDARY GRAD–SHAFRANOV EQUILIBRIUM

The design-point equilibrium is reconstructed with FreeGS/FreeGSNKE [21,22], which solve the free-boundary Grad–Shafranov equation

$$\Delta^*\psi \equiv R^2\nabla\cdot\left(\frac{\nabla\psi}{R^2}\right) = -\,\mu_0 R^2\,p'(\psi) - I(\psi)\,I'(\psi),$$

on a 129×129 (R,Z) grid with an eight-coil poloidal-field set plus solenoid. The elliptic operator Δ^* is discretized with a second-order five-point stencil; the Picard fixed-point iteration alternates a fast Poisson solve for ψ with an update of the toroidal current $j_\phi = Rp' + II'/(\mu_0 R)$, converging to relative tolerance 10^{-6}. Shape is pinned by a 16-point isoflux constraint on the Miller negative-triangularity boundary ($R_0 = 1.20\,\mathrm{m}$, $a = 0.48\,\mathrm{m}$, $\kappa = 2.0$, $\delta = -0.30$) and (β_p, I_p) by a `ConstrainBetapIp` control with $\beta_p = 0.37125$ and $I_p = 9.66$ MA. The solve reproduces $I_p = 9.660$ MA, $\beta_p = 0.3712$ and plasma volume $13.84\,\mathrm{m}^3$, byte-consistent with the independent equilibrium archive [31].

Ideal-MHD stability is evaluated on 19 flux surfaces $\psi_N = 0.05$–0.95. The local interchange (Mercier) criterion is computed from the shaped-equilibrium q, magnetic shear $\hat{s} = (r/q)\,\mathrm{d}q/\mathrm{d}r$ and pressure gradient in the large-aspect Suydam form

$$D_M = \frac{\hat{s}^2}{4r} + \frac{2\mu_0(1-q^2)}{B_0^2}\frac{\partial p}{\partial r}, \qquad \text{stable} \;\Leftrightarrow\; D_M > 0,$$

cross-checked against the traced flux-surface-averaged magnetic well $\mathrm{d}U/\mathrm{d}\psi$ and $\langle B^2\rangle$. Infinite-n ballooning stability uses the Connor–Hastie–Taylor s–α operator [14]

$$\mathcal{B}[F] = -\frac{\mathrm{d}}{\mathrm{d}\theta}\left[(1+\Lambda^2)\frac{\partial F}{\partial\theta}\right] - \alpha(\cos\theta + \Lambda\sin\theta)F, \qquad \Lambda = \hat{s}\theta - \alpha\sin\theta,$$

with $\alpha = -2\mu_0 q^2 R_0(\mathrm{d}p/\mathrm{d}r)/B_0^2$, solved as a symmetric-tridiagonal ground-state eigenproblem on $\theta\in[-6\pi, 6\pi]$ with $N = 3000$ nodes; instability is signalled by a negative smallest eigenvalue. The solver reproduces the classic first-stability boundary $\alpha_{\mathrm{crit}} \approx 0.6$ at $\hat{s} = 1$.

DRIFT-KINETIC BOOTSTRAP: NEO SPECTRAL DISCRETIZATION

The bootstrap current is computed with the GACODE drift-kinetic solver NEO [12,13], which discretizes equation (7) in a spectral basis: Legendre polynomials in pitch angle $\xi = v_\parallel/v$ (order $N_\xi = 17$), an energy grid ($N_E = 8$), and a Fourier/spline poloidal representation ($N_\theta = 25$), with the full linearized Fokker–Planck collision operator (`COLLISION_MODEL=4`) and kinetic electrons on Miller geometry (`EQUILIBRIUM_MODEL=2`). Runs use two MPI ranks within a bounded CPU budget; the physical collisionality and normalized gyroradius are set from the config-22021 anchors ($R_0/a = 2.5$, $\kappa = 2.0$, $\delta = -0.30$, $n_e = 4.0\times10^{20}\,\mathrm{m}^{-3}$, $T_i = 15(1-\rho^2)\,\mathrm{keV}$, $B_{\mathrm{unit}} \approx 16\,\mathrm{T}$). Three local radii $r/a = 0.5, 0.6, 0.7$ are solved; the parallel current is normalized identically to the Sauter comparison ($\langle j_\parallel B\rangle/B_{\mathrm{unit}}$, in $e\,n_e c_s$ units) so the ratio is definitional rather than a units artifact.

TURBULENCE, EXTENDED-MHD AND ERROR-FIELD REFERENCES

The marginal linear growth rate entering equation (6) is taken from the companion nonlinear/linear gyrokinetic study run with CGYRO [17,18,32], an Eulerian gyrokinetic–Maxwell solver executed on the GPU campaign; the quiet-basin threshold $a/L_{T,\mathrm{crit}} \approx 2.1$ and the 31–60% negative-triangularity growth-rate reduction come from those runs. The disruption current-quench window (§4.5) is grounded in an extended-MHD model built with NIMROD [20]: the frozen breeder equilibrium was read from its EFIT geometry and verified against every design parameter ($R_0 = 1.203\,\mathrm{m}$, $a = 0.473\,\mathrm{m}$, $B_0 = -7.98\,\mathrm{T}$, $I_p = 9.62\,\mathrm{MA}$, $\kappa = 1.971$, $\delta = -0.29$), made finite-element-consistent and force-balanced, and its full current transferred into the evolving $n = 0$ field. The resistive semi-implicit advance did not converge to a dynamic quench on this build, so the current-quench time is reported honestly as an L/R estimate grounded in the verified equilibrium, not a time-advance (§6). The $2/1$ error-field threshold uses the Buttery-class empirical scaling of equation (11) with an intrinsic-field tolerance stack; it is not a resistive-MHD penetration solve, and is labelled as such.

VERIFICATION AND REPRODUCIBILITY

Every metric was cross-checked against an independent route: the equilibrium against the archived reconstruction [31]; the ballooning eigensolver against the analytic s–α boundary; the Mercier sign balance against the traced magnetic well; the NEO bootstrap against three analytic models (Hirshman–Hinton, Koh, Sauter-modified) at $r/a = 0.6$. The stability margins, bootstrap ratios and disruption window are frozen entries (BR-L2-A19, BR-L2-A16, BR-L2-A10, BR-CX-33, BV-03, KFE-CF-BR-006, KFE-CF-BR-015) of the de-risking register [30] and regenerate from the free-boundary and drift-kinetic archives deposited with this paper. The figure data are emitted by a single uniquely-named script bundled in the deposit.

§ 4

Results

THE STABILITY BASE AND THE BINDING CONSTRAINT

The reconstructed equilibrium carries a peaked core current ($q_0 \approx 0.34$, internal inductance $\ell_{i3} = 1.40$) with the $q = 1$ surface at $\psi_N \approx 0.72$ and $q_{95} = 2.90$ (Figure 1). The confinement region — every surface outside $q = 1$ — is the operationally relevant zone, and it is unconditionally stable in the two local metrics. The Mercier criterion (Figure 2) is violated only on the seven surfaces inside $q = 1$, an artifact of the peaked `ConstrainBetapIp` core (a physical sawtooth-relaxed profile clamps $q_0 \to 1$ and removes the drive); on the confinement region D_M grows monotonically from $+0.23$ at $\psi_N = 0.40$ to $+47$ near the edge. Infinite-n ballooning (Figure 3) is unstable only in a small low-shear core pocket ($\psi_N = 0.15$–0.25, again inside $q = 1$); the confinement region is in first stability with the pressure-gradient parameter capped at $\alpha_{\max} \approx 0.55$, far below the s–α boundary wherever shear is appreciable. Because negative triangularity improves the local field-line curvature and the s–α model does not capture that improvement, the ballooning verdict is conservative.

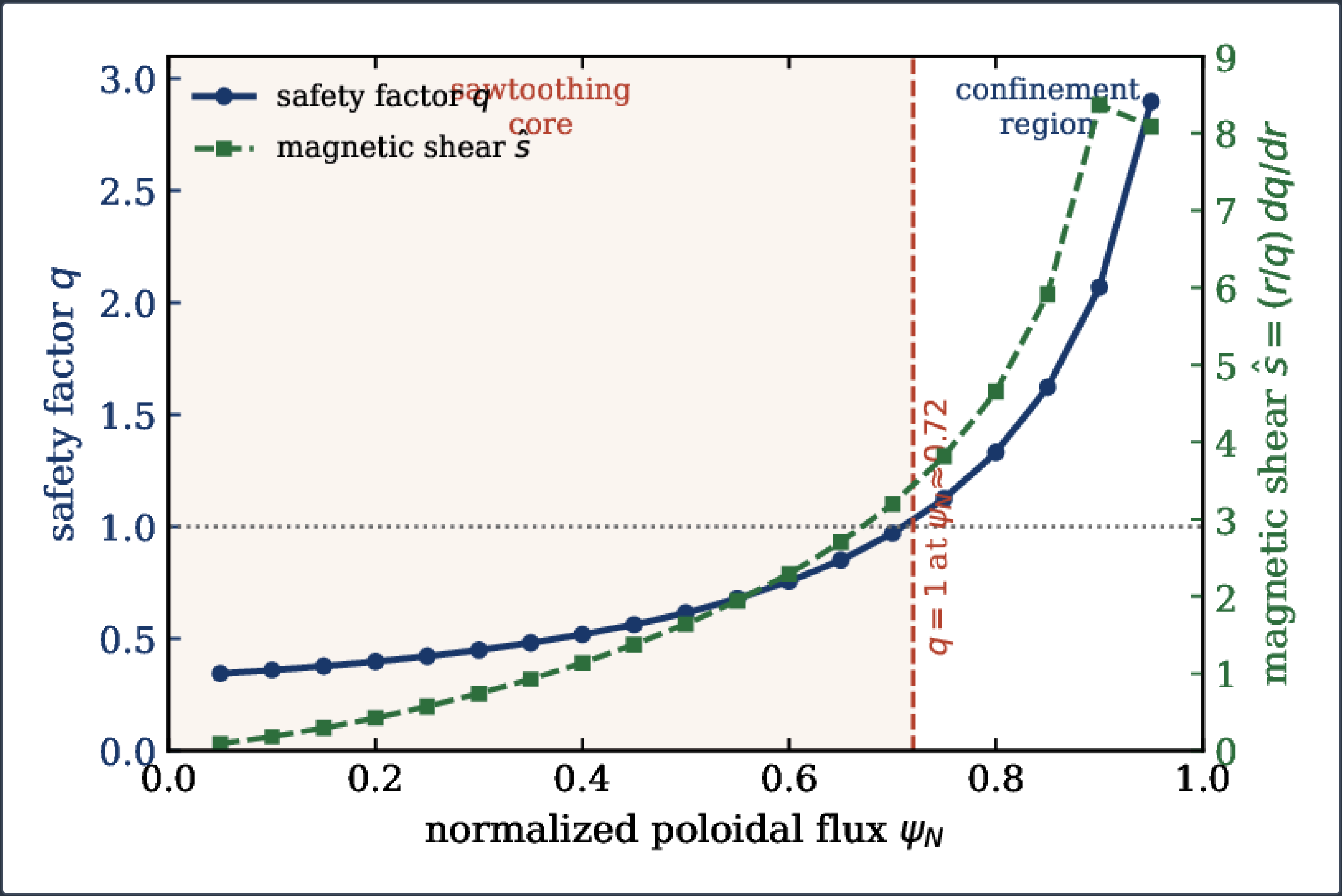

Safety factor $q(\psi_N)$ and magnetic shear $\hat{s}(\psi_N)$ from the free-boundary reconstruction (BR-L2-A19). The $q = 1$ surface at $\psi_N \approx 0.72$ separates the peaked sawtoothing core from the confinement region; $q_{95} = 2.90$.

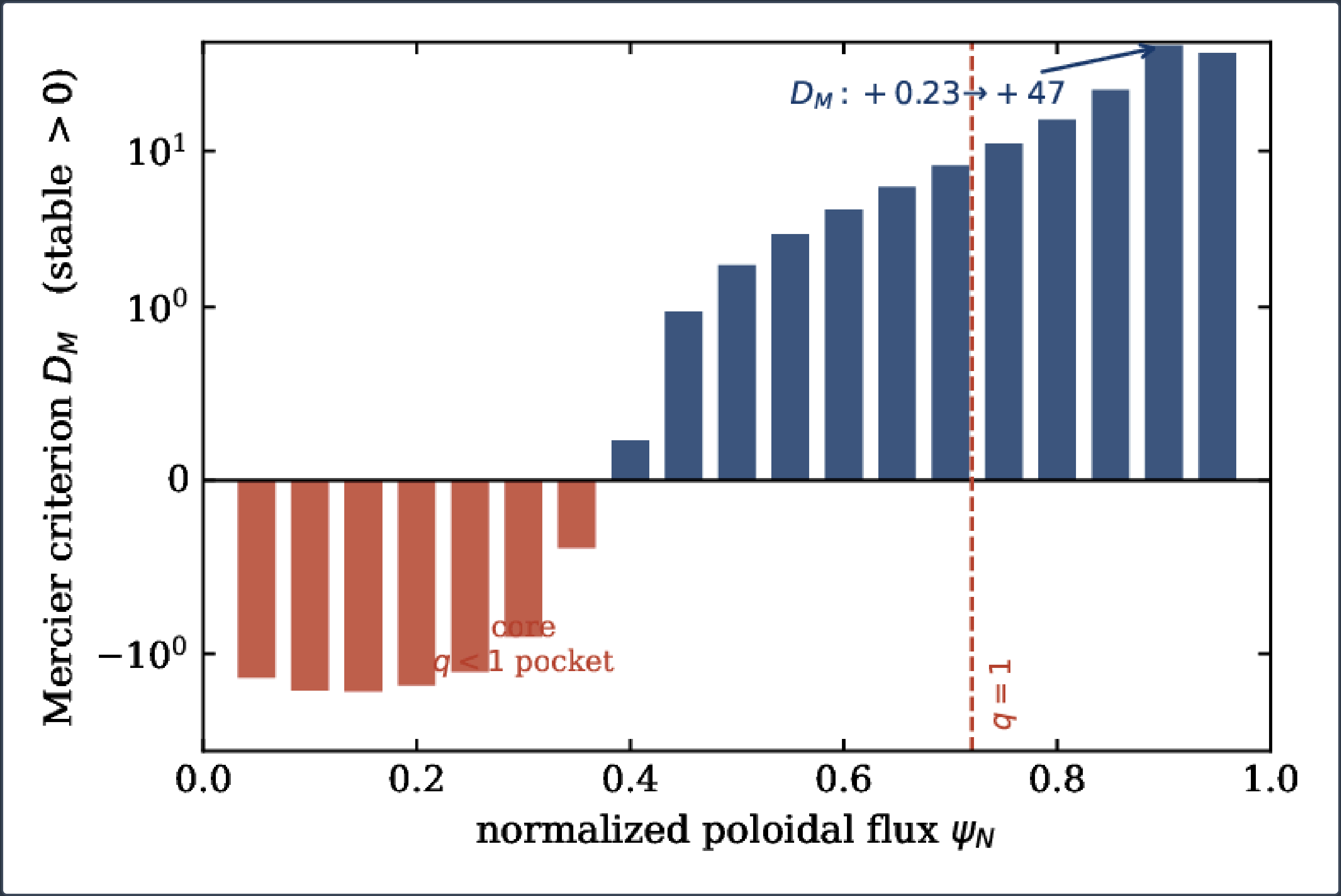

Mercier interchange criterion $D_M(\psi_N)$ (symmetric-log axis; stable for $D_M > 0$). Violations (red) lie entirely inside $q = 1$; on the confinement region the margin grows from $+0.23$ to $+47$ toward the edge (BR-L2-A19).

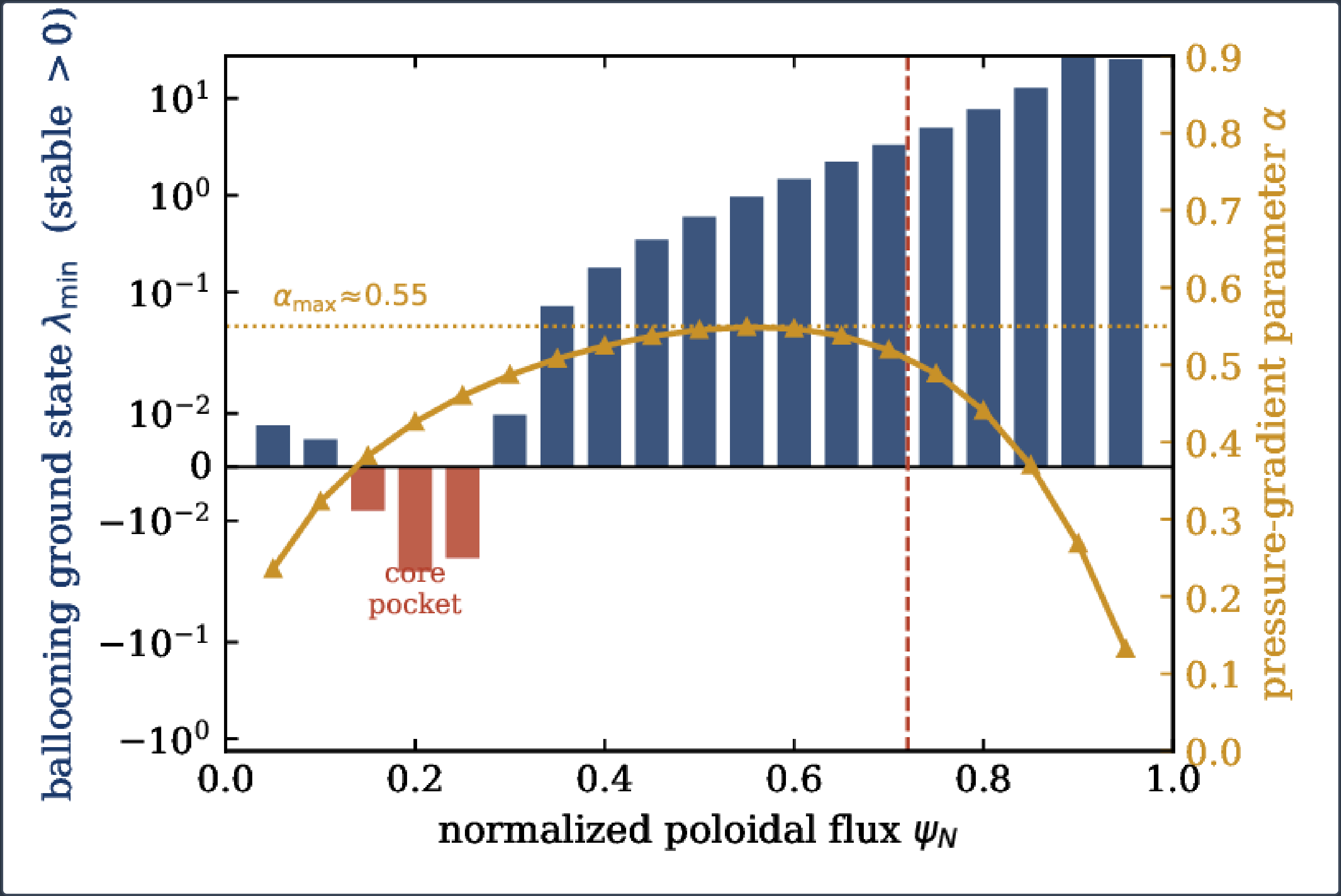

Infinite-n ballooning ground-state eigenvalue $\lambda_{\min}(\psi_N)$ (bars, stable > 0) and pressure-gradient parameter $\alpha(\psi_N)$ (line). The confinement region is in first stability with $\alpha_{\max} \approx 0.55$; the only instability is a low-shear core pocket inside $q = 1$ (BR-L2-A19).

The binding constraint is the global $n = 1$ external kink (Table 1, Figure 4). On the standard definition the normalized beta is $\beta_N = 2.13$, which sits below the no-wall Troyon coefficient $g = 2.8$ with a margin of $1.31\times$ and below the ideal-wall value $g = 3.5$ with $1.64\times$; on the free-boundary code's native beta definition (2.44) the same margins read a more conservative $1.15\times$ and $1.43\times$, and the 0-D anchor ($\beta_N = 1.53$) gives $1.83\times$ to the no-wall limit. The external kink is therefore stable without a conducting wall, but by the smallest of the three margins — and because negative triangularity modestly lowers the Troyon coefficient, the no-wall margin is a real caution rather than a conservative one. This is precisely the regime in which equation (9) says rotation and wall coupling carry operational weight.

METRIC	RESULT ON THE CONFINEMENT REGION	MARGIN
Mercier interchange	stable for all $\psi_N > 0.72$; $D_M : +0.23 \to +47$	wide, growing edgeward
infinite-n ballooning	first-stability stable; $\alpha_{\max} \approx 0.55$	well below s–α boundary
$n = 1$ external kink	$\beta_N = 2.13$ below no-wall Troyon ($g = 2.8$)	$1.31\times$ **(binding)**
$n = 1$ external kink	$\beta_N = 2.13$ below ideal-wall ($g = 3.5$)	$1.64\times$

Ideal-MHD stability of the design-point negative-triangularity equilibrium (BR-L2-A19). The $n = 1$ kink is the binding constraint.

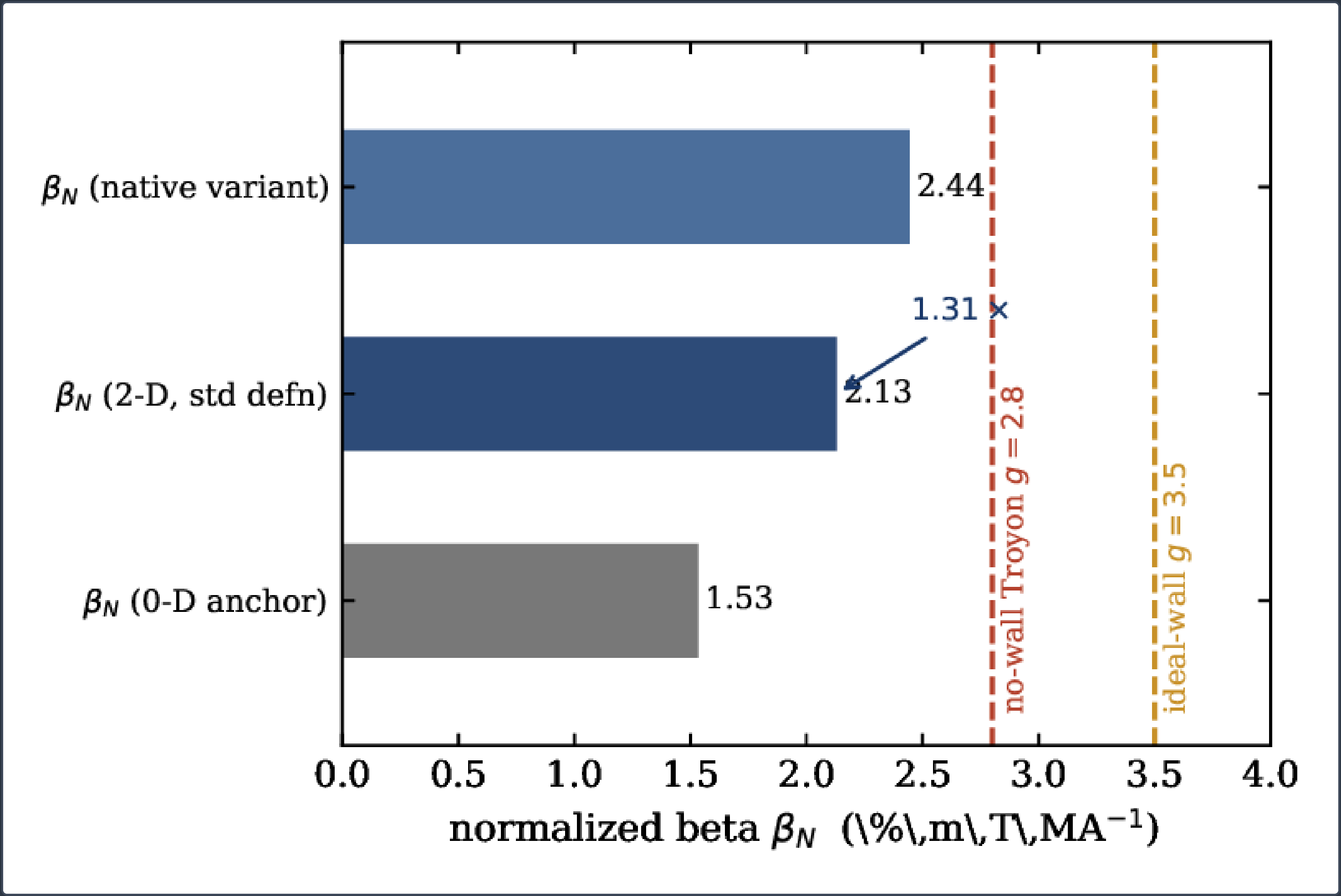

The operating β_N (standard **2.13**, native variant **2.44**, **0**-D anchor **1.53**) against the no-wall Troyon limit ($g = 2.8$) and the ideal-wall limit ($g = 3.5$). The band between the two dashed lines is where equation (9) makes the RWM unstable and rotation plus wall coupling stabilize it (BR-L2-A19).

ROTATION FROM FIRST PRINCIPLES

The rotation and current profile that the flow-shear controller shapes are anchored in the drift-kinetic solve rather than an analytic fit. Solving equation (7) with the full Fokker–Planck operator and kinetic electrons gives a parallel bootstrap current that runs consistently below the Sauter closure of equation (8): the NEO/Sauter ratio is **0.811**, **0.843** and **0.873** at $r/a = 0.5$, **0.6** and **0.7** (Table 2, Figure 5). The collisionality there, $\nu_e^* \approx 0.012$, is squarely in the banana regime — exactly where the Sauter fit is known to over-predict — so the $\approx 17\%$ reduction is real physics, not a numerical artifact, and it reproduces the register's "$\sim 83\%$ of Sauter" figure. Three independent analytic models at $r/a = 0.6$ bracket the result (Hirshman–Hinton 4.05×10^{-3}, banana-limit only; Koh $1.235 \times 10^{-2} \approx$ Sauter; Sauter-modified 1.155×10^{-2}), placing NEO between the deep-banana and Sauter estimates as expected. A bootstrap fraction of this size sets the intrinsic current, and through the diamagnetic term of equation (4) the radial electric field that seeds the flow shear of §4.3.

r/a	$\langle j_\parallel B \rangle$ NEO	$\langle j_\parallel B \rangle$ SAUTER	NEO/SAUTER	ν_e^*
0.5	7.21×10^{-3}	8.89×10^{-3}	0.811	~ 0.012
0.6	1.04×10^{-2}	1.24×10^{-2}	0.843	~ 0.012
0.7	1.52×10^{-2}	1.74×10^{-2}	0.873	~ 0.012

First-principles neoclassical bootstrap current versus the Sauter model (BR-L2-A16, drift-kinetic NEO, full Fokker–Planck, kinetic electrons). Normalization $\langle j_\parallel B \rangle / B_{\text{unit}}$ in $e\, n_e c_s$ units.

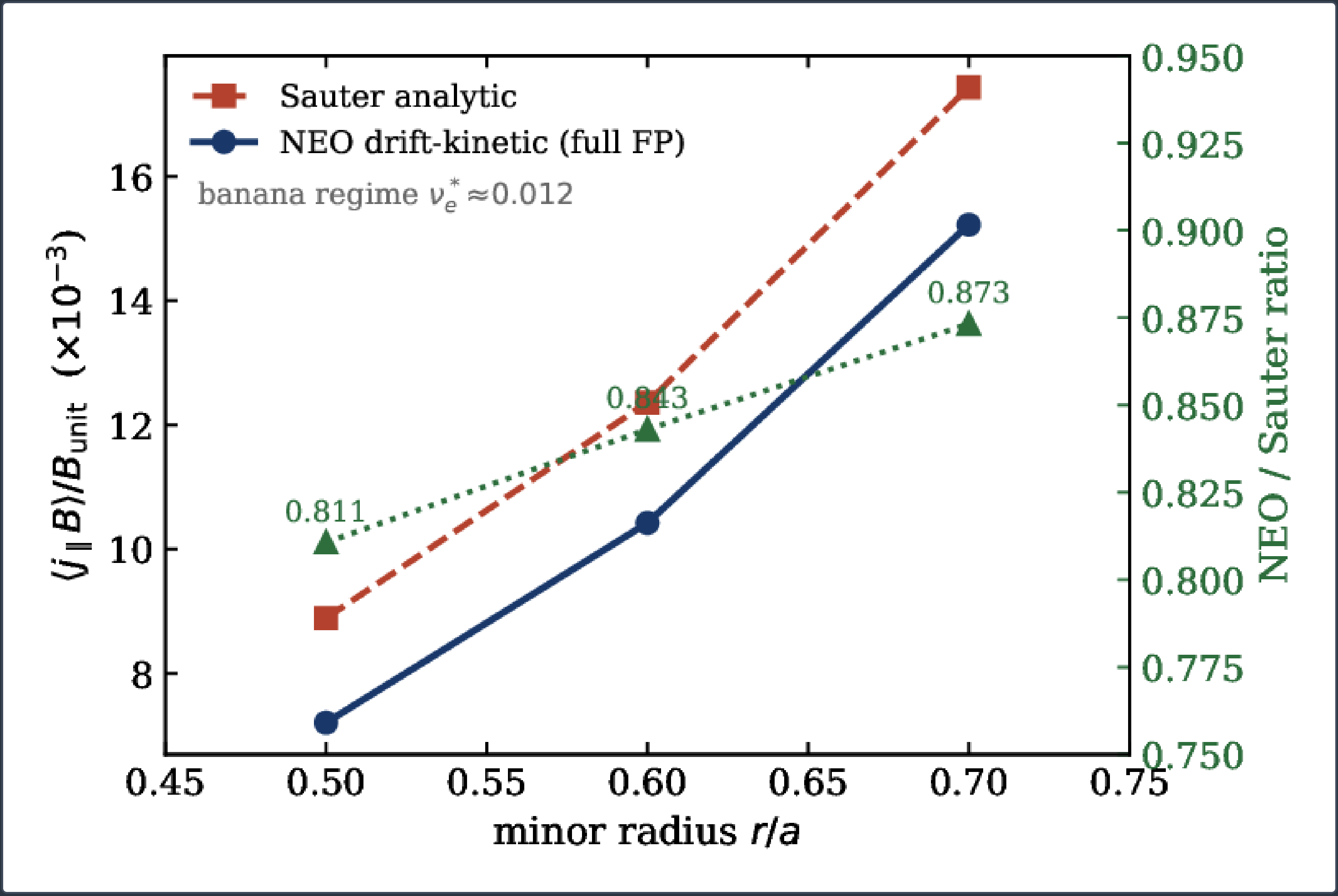

Parallel bootstrap current from first-principles drift-kinetic NEO (blue) versus the Sauter analytic closure (red) across $r/a = 0.5$–0.7; the NEO/Sauter ratio (green) is 0.81–0.87 in the banana regime ($\nu_e^* \approx 0.012$), where Sauter over-predicts (BR-L2-A16).

THE FLOW-SHEAR SUPPRESSION WINDOW

Figure 6 evaluates the suppression criterion of equation (6) from the frozen equilibrium. Taking the diamagnetic term of equation (4) with the reconstructed pressure gradient and the flat density $n_e = 4.0 \times 10^{20}\ \mathrm{m}^{-3}$, the reduced-model $E \times B$ shearing rate γ_E of equation (5) rises steeply through the confinement region and exceeds a representative marginal growth-rate band ($\gamma_{\max}^{\mathrm{lin}} \sim (1\text{–}3) \times 10^5\ \mathrm{s}^{-1}$, from the companion CGYRO quiet basin [32]) over the outer half of the plasma. This is a reduced-model estimate, not a measured shearing rate: it fixes the target the controller must maintain, and it shows the target is reachable with the intrinsic diamagnetic field alone. The controller's job is then narrow and falsifiable — hold $\gamma_E \gtrsim \gamma_{\max}^{\mathrm{lin}}$ under disturbances — because the negative-triangularity shape has already lowered the right-hand side.

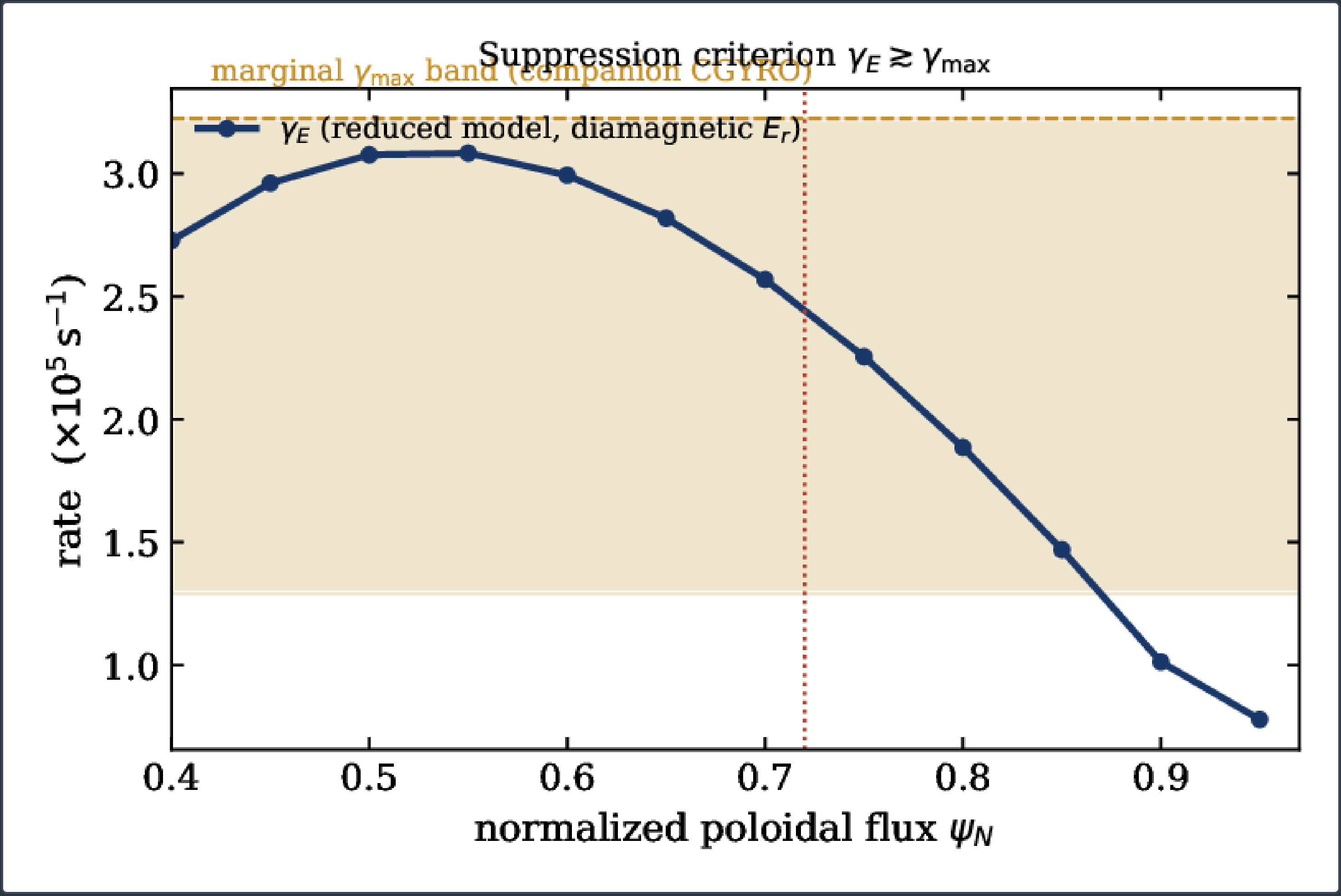

(Reduced model.) $E \times B$ shearing rate $\gamma_E(\psi_N)$ computed from the frozen-equilibrium diamagnetic radial electric field (equations 4–5), against a representative marginal linear growth-rate band from the companion nonlinear-gyrokinetic study [32]. The suppression criterion $\gamma_E \gtrsim \gamma_{\max}^{\mathrm{lin}}$ (equation 6) is met over the outer confinement region.

ERROR-FIELD TOLERANCE AND LOCKED-MODE AVOIDANCE

The two sides of the locked-mode inequality $b_r < b_{\rm th}$ are quantified in Figure 7. The empirical scaling of equation (11) at canon conditions ($n_e = 4.0 \times 10^{20}\ \mathrm{m}^{-3}$, $B_T = 8\,\mathrm{T}$) raises the $2/1$ penetration threshold to $b_{\rm th} \approx 9.8 \times 10^{-4}$: the compact high-density breeder is intrinsically error-field tolerant, because the same density that carries the fusion power also stiffens the plasma against reconnection in equation (10). The intrinsic resonant field, estimated from a coil-assembly tolerance stack with coupling $b_r \simeq k(\delta r/R_0)$, $k \sim 0.5$, is 2.1×10^{-4}, 4.2×10^{-4} and 8.3×10^{-4} at 0.5, 1.0 and 2.0 mm assembly, giving margins of $4.7\times$, $2.3\times$ and $1.2\times$. At ≤ 1 mm coil assembly the intrinsic field stays a factor 2.3 below the threshold. Combined with the negative-triangularity edge, which is ELM-free and needs no resonant magnetic perturbation for edge control [38], this makes RMP-free operation feasible: dedicated correction coils are not load-bearing for the baseline, though trim/error-field-correction coils remain prudent insurance for assembly outliers and the 2 mm case where the margin thins to $1.2\times$.

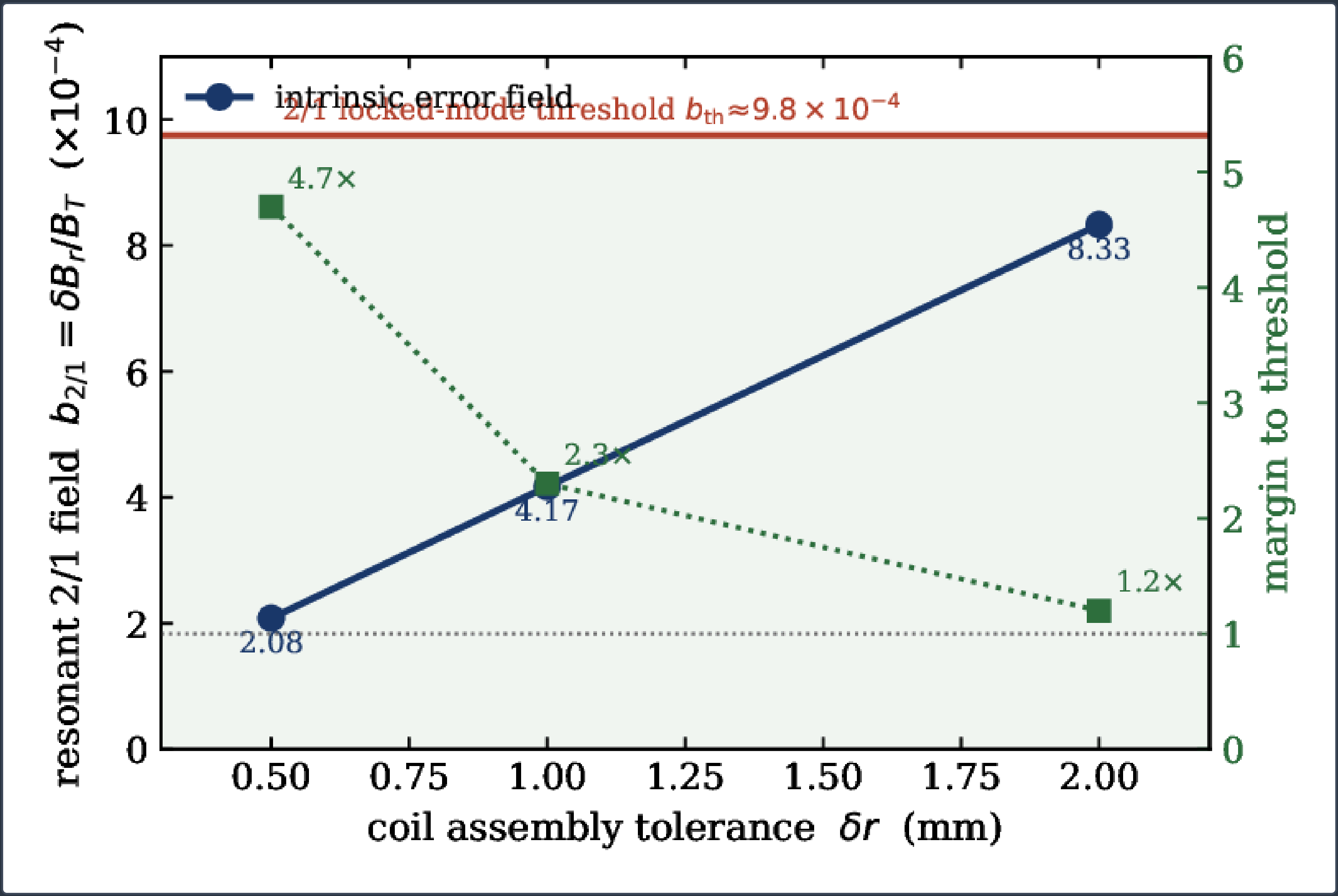

$2/1$ locked-mode penetration threshold $b_{\rm th} \approx 9.8 \times 10^{-4}$ (red line) from the density–field scaling of equation (11), against the intrinsic resonant field (blue) at $0.5/1.0/2.0$ mm coil assembly and the resulting margin (green). At ≤ 1 mm the margin is $2.3\times$; RMP-free operation is feasible (BR-CX-33).

VERTICAL STABILITY AND CLOSED-LOOP ARREST

The rotation-independent third leg is the vertical mode. The rigid-shift analysis gives an open-loop stability index $\gamma_z \tau_w = 8.05$; with a stainless-steel vessel wall time $\tau_w \approx 11.9$ ms this is a growth rate $\gamma_z \approx 677\,\mathrm{s}^{-1}$ (growth time 1.5 ms). The PD controller of equation (12) is Hurwitz-stable above $K_p \gtrsim 3.0 \times 10^4\,\mathrm{V\,m}^{-1}$; the closed loop places a fast pole at $-964\,\mathrm{s}^{-1}$ (instability arrest) and a slow pole at $-14\,\mathrm{s}^{-1}$ (resistive coil-flux relaxation, removed by the integral/equilibrium coils), arresting a 5 mm vertical disturbance in 3.5 ms (Figure 8). The required poloidal-field converter authority is ~ 49 MVA at 10 kV and $5\,\mathrm{kA\,ms}^{-1}$. Because an unarrested vertical-displacement event terminates in a disruption exactly as a locked mode does, the vertical controller belongs in the same locked-mode-avoidance layer and shares its acceptance philosophy; its detailed design is developed in the dedicated vertical-stability study [35].

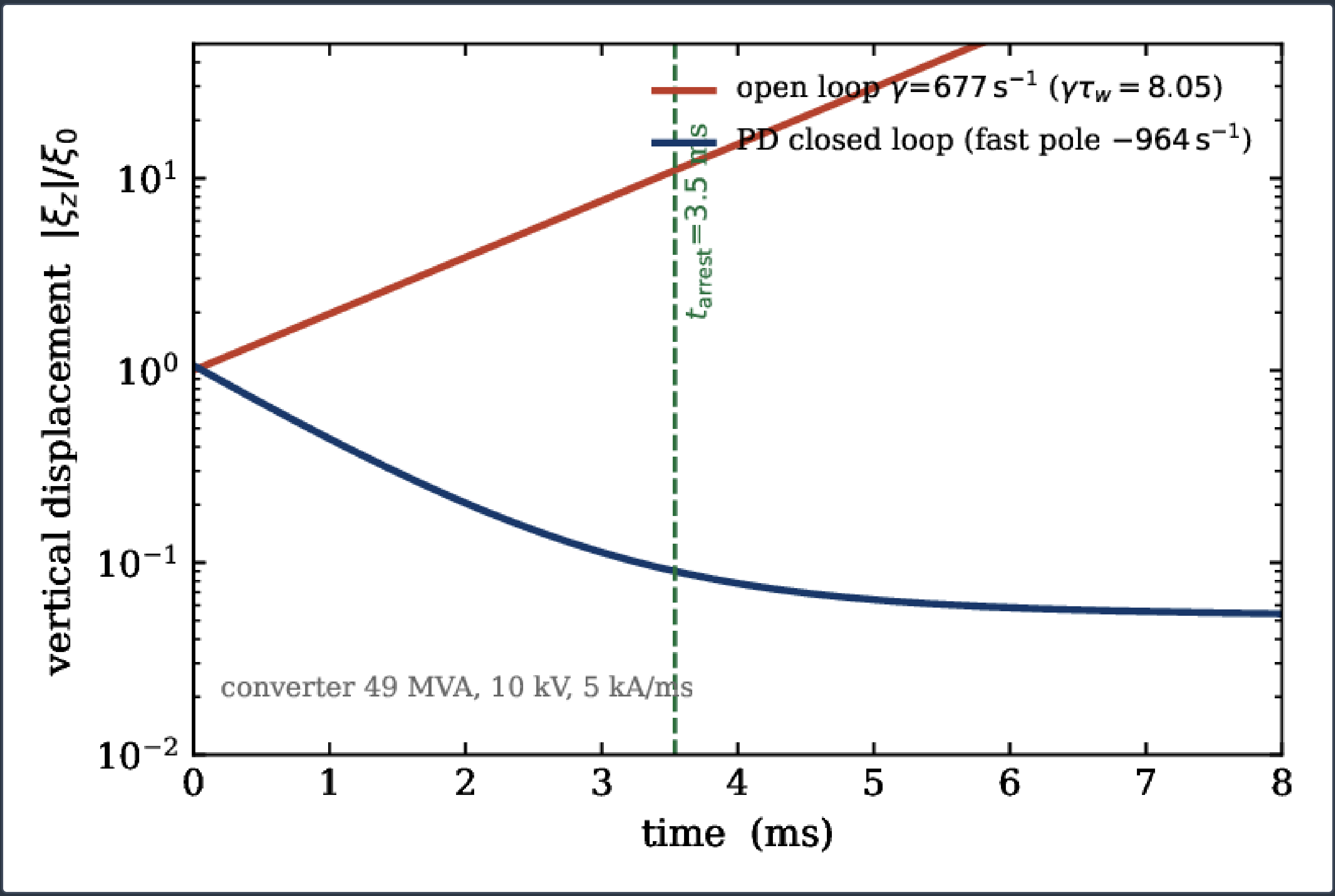

Vertical-displacement evolution (log axis). Open loop grows at $\gamma_z = 677\,\mathrm{s}^{-1}$ ($\gamma_z \tau_w = 8.05$); the PD closed loop (fast pole $-964\,\mathrm{s}^{-1}$) arrests a 5 mm disturbance in 3.5 ms with a ~ 49 MVA converter (BV-03).

THE ROTATION, FLOW-SHEAR AND ERROR-FIELD CONTROL LAYER

On this stable, well-characterized base the control layer has a well-posed job (Figure 9, Table 3). It comprises three coordinated elements, each specified with an acceptance test set in advance. The flow-shear/rotation controller drives sheared $E \times B$ flow to hold turbulence suppressed (equation 6) and keeps the plasma rotating fast enough that, should a beta excursion enter the RWM band of equation (9), wall coupling stabilizes the mode. The tearing/locked-mode detector with electron-cyclotron current drive catches and suppresses seeded tearing modes before the rotation collapse of equation (10) can lock them. The vertical-stability PD controller of equation (12) closes the axisymmetric loop. Beneath all three sits a deterministic, worst-case-bounded certified clamp that hands authority to a hardware fail-safe out of distribution, consistent with the Kronos real-time control architecture [37].

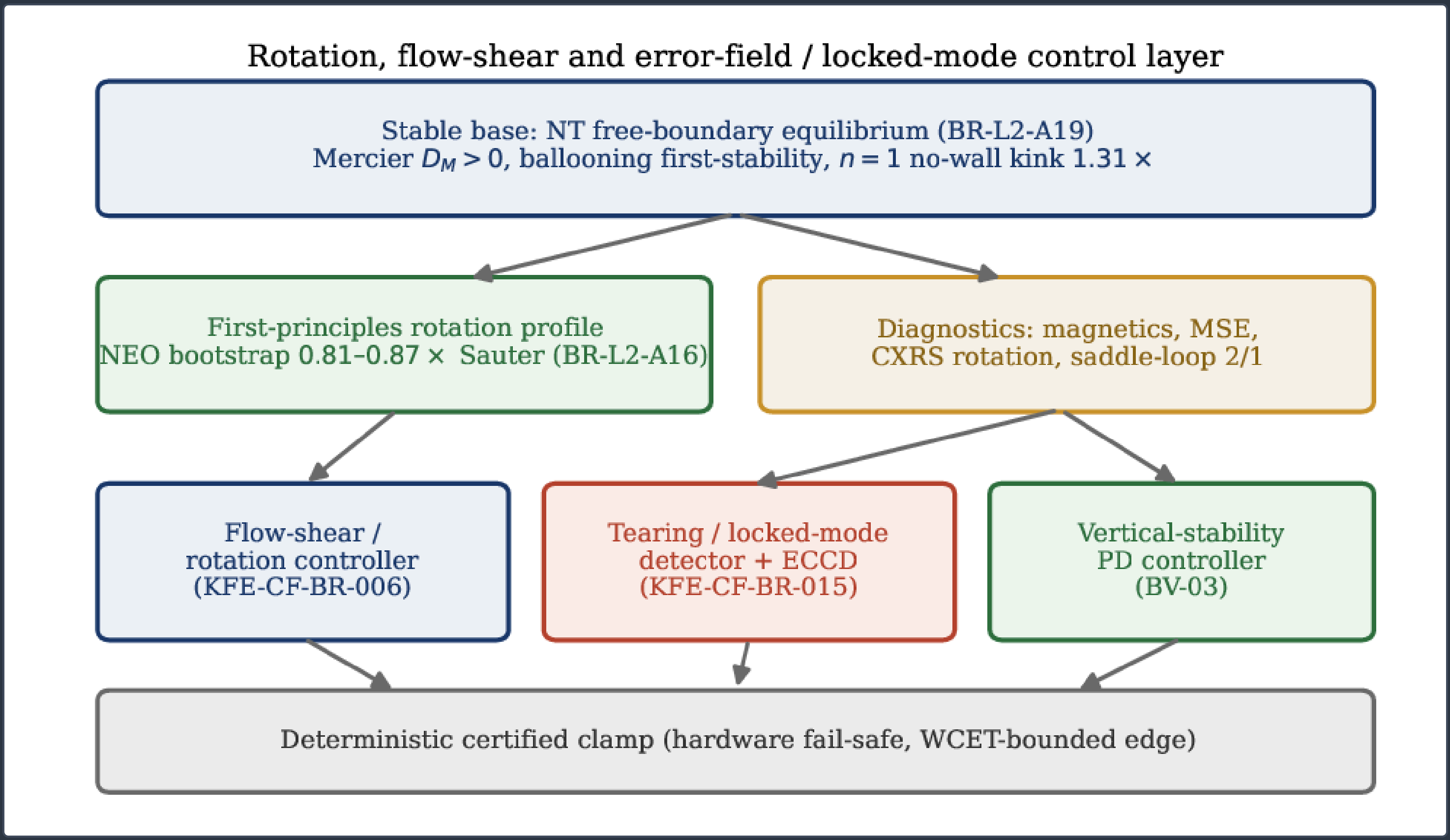

(Schematic.) The rotation, flow-shear and error-field / locked-mode control layer: a stable equilibrium base and a first-principles rotation profile feed three controllers (flow-shear, tearing/locked-mode, vertical stability), all beneath a deterministic certified clamp.

P5.0CMP4.2CM ELEMENT	ACCEPTANCE CRITERION	FEATURE TEST
flow-shear / rotation controller	closed-loop stable to setpoint within tolerance; disturbance rejected; zero certified-clamp trips in nominal operation	turbulence suppression tracks the rotation setpoint against the gyrokinetic reference
tearing / locked-mode detector + ECCD	catch rate and lead-time meet target; the clamp acts before loss of control on every seeded event	suppresses seeded tearing modes in simulation
vertical-stability PD controller	closed-loop poles in the left half-plane; 5 mm disturbance arrested $<$ growth time	displacement arrested in 3.5 ms with ≤ 49 MVA converter

Control-layer elements and their pre-set acceptance criteria (register serials KFE-CF-BR-006, KFE-CF-BR-015, and the vertical-stability controller BV-03).

§ 5

Discussion

The negative-triangularity design earns its quiet core, and this work shows both why that core is stable and what holds it stable near its one binding limit. Placed against the published literature, each element is quantitatively consistent. The no-wall external-kink margin of $1.31\times$ at $\beta_N = 2.13$ is the regime for which Bondeson and Ward [1] and the ITER Physics Basis [15] prescribe rotation plus wall coupling; the design sits just inside the no-wall boundary, so it does not require rotational RWM stabilization nominally, but equation (9) shows a same-size excursion enters the band, which is why the rotation cushion is specified rather than assumed. The bootstrap reduction to 0.81–$0.87\times$ Sauter is exactly the banana-regime over-prediction that motivated the drift-kinetic NEO development [12,13]: our $\nu_e^* \approx 0.012$ places the plasma in the deep-banana regime where the $\mathcal{L}_{3k}(f_t, \nu_e^*)$ coefficients of equation (8) are least reliable, and the $\sim 17\%$ correction is in line with published NEO-versus-Sauter comparisons. The error-field tolerance follows the Buttery scaling [8] evaluated at a density (4×10^{20} m $^{-3}$) well above conventional tokamaks, so the raised threshold $b_{\mathrm{th}} \approx 9.8 \times 10^{-4}$ and the resulting $2.3\times$ margin at 1 mm assembly are the expected consequence of a compact high-density design, not an optimistic outlier; the value is comparable to the $\delta B/B \sim 10^{-4}$ sensitivity Buttery infers for ITER, with our margin coming from the higher density. Anchoring the rotation in first-principles neoclassics rather than an analytic bootstrap model removes a systematic bias from the current profile the controller shapes, so the control layer is built on a transport base that is correct at the level that matters. The result is a coherent stack: a stable equilibrium, a first-principles rotation profile, and a specified control layer with falsifiable acceptance tests, each tied to a frozen register entry.

§ 6

Limitations

Three gates are stated honestly and left open. First, the stability assessment resolves the local interchange and infinite-n ballooning spectra directly, but the global $n = 1$ margin is a Troyon-coefficient comparison, not an eigenvalue; the owed computation is a global δW eigenvalue solve (DCON/MARS-class) that converts the kink margin into a full RWM eigenmode with its rotation and wall-coupling terms, queued for the global-mode toolchain. Second, the disruption current-quench window $\tau_{\text{CQ}} \approx 7\text{–}19$ ms is an L/R estimate grounded in the finite-element-consistent, ideal-stable NIMROD equilibrium; the resistive semi-implicit advance did not converge to a dynamic quench on the present build, so no simulated τ_{CQ} was obtained and none is claimed. Third, the $E \times B$ suppression window (Figure 6) and the error-field threshold (equation 11) are reduced-model and empirical respectively — the former uses the diamagnetic E_r without the full poloidal-flow and neoclassical offset of equation (4), and the latter is a multi-machine scaling rather than a resistive-MHD (M3D-C1/MARS-F) penetration solve for this specific negative-triangularity equilibrium. None of the three changes the qualitative picture; each is a fidelity upgrade, not a reversal.

§ 7

Conclusion

The Hyperion breeder equilibrium is ideal-MHD stable across its confinement region — Mercier-stable with margins growing to $+47$, ballooning-stable at $\alpha_{\max} \approx 0.55$ — with the $n = 1$ no-wall kink the binding constraint at $\beta_N = 2.13$ and a $1.31\times$ margin. Rotation, flow-shear and error-field correction are the layer that holds that near-limit point. A first-principles drift-kinetic bootstrap current at 0.81–$0.87\times$ Sauter in the banana regime anchors the rotation profile; the diamagnetic radial electric field it carries drives an $E \times B$ shearing rate that meets the turbulence-suppression criterion over the outer confinement region; the high operating density raises the $2/1$ locked-mode threshold to 9.8×10^{-4} so that a ≤ 1 mm coil assembly leaves a $2.3\times$ margin and RMP-free operation is feasible; and a PD vertical-stability controller arrests a 5 mm displacement in 3.5 ms. On this base a flow-shear controller, a tearing/locked-mode detector with electron-cyclotron current drive, and the vertical controller close the turbulence-suppression, locked-mode-avoidance and vertical-stability loops with explicit acceptance criteria. The design is stable by construction and held stable by design.

Acknowledgments tocsectionAcknowledgments Part of the Kronos Fusion Energy 2026 design series. The authors thank the Kronos physics de-risking campaign for the frozen equilibrium, drift-kinetic, gyrokinetic and extended-MHD archives that ground this work, and acknowledge the NVIDIA GPU HPC campaign on which those calculations were run.

Reproducibility. The stability margins, neoclassical bootstrap ratios, error-field tolerance stack, vertical-stability indices and disruption current-quench window are frozen entries (BR-L2-A19, BR-L2-A16, BR-CX-33, BV-03, BR-L2-A10, KFE-CF-BR-006, KFE-CF-BR-015) in the Kronos Physics De-Risking Register and are regenerable from the free-boundary, drift-kinetic and extended-MHD archives with this paper. This paper is archived at doi:10.5281/zenodo.22645907; official version: https://www.kronosfusionenergy.com/publications/toroidal-rotation-flow-shear-stabilization-and-error-fi.html and the register at doi:10.5281/zenodo.22133057.

Data availability tocsectionData availability This paper is archived at doi:10.5281/zenodo.22645907. The free-boundary equilibrium arrays, stability spectra, NEO bootstrap outputs, error-field tolerance stack and vertical-stability results, together with the single figure-generation script, are archived with the deposit and reference the Kronos 2026 series. Any economic analysis is reported separately and is not part of the public deposit.

Competing interests tocsectionCompeting interests Provisional patent applications relating to aspects of this work have been filed. The authors declare no other competing interests.

APPARATUS

Portfolio, People & Record

The intellectual-property estate, the people who built it, the limitations that gate it, and the sources it rests on.

1	4	40	27
GRANTED PATENT	2026 PROVISIONALS	TEAM MEMBERS	2022 PROVISIONALS

INTELLECTUAL PROPERTY

The patent portfolio

The estate spans a granted high-field magnet patent, pending utility and 2026 provisional filings that map to the two products, a digital-twin control provisional, a registered trademark application, and the original 2022 provisional family. Every patentable disclosure in the five-paper arXiv drop was protected **before** publication: the breeder and burner provisionals were filed 1–2 August, and a publication-gap omnibus filing the evening before the drop swept up the DEC, plasma-control, and REBCO-winding matter of the three otherwise-unprotected papers. Patent numbers and application serials are matters of public record; claim scope is summarised, not reproduced.

GRANTED & PENDING UTILITY

US 12,009,112	High-field tilted graded-REBCO magnet architecture (KRONO-002A) · *app. 17/878,550*	GRANTED
US 17/878,507	Core device / method (KRONO-001A) · *utility*	PENDING

2026 PROVISIONAL FILINGS — MAPPED TO THE PRODUCTS

64/124,209	Hyperion — spherical-tokamak tritium / helium-3 foundry · *breeder · filed Aug 2026*	FILED
64/124,220	Aegis / MetroVolt — synchrotron-cutoff, fuel-selection & plug-winding · *generator · filed Aug 2026*	FILED
64/115,167	KRONOS-CTRL digital-twin plant control · *provisional · filed Jul 2026*	FILED
64/005,440	Integrated spherical-tokamak fusion architecture · *early integrated-architecture filing · filed Mar 2026*	FILED
64/105,530	Negative-triangularity spherical-tokamak architecture · *foundational ST filing · filed Jul 2026*	FILED
64/128,097	Publication-gap omnibus — quasineutral two-species expander DEC · provenance-gated / latency-split plasma control · as-built high-field winding & conductor architecture · *filed 7 Aug 2026, the evening before the arXiv drop*	FILED

TRADEMARK & ORIGIN

FTK-98801894	Kronos Fusion Energy — trademark application	FILED
KR-2022-*	Original provisional family (KR-2022-00001 … 00027) · *27 filings, 2022*	PRIORITY

The narrow, defensible magnet novelty — the specific conductor and the digital-twin winding optimisation, not high-field REBCO as a category — is the commercial core that can earn ahead of any Q > 1 milestone, with markets in fusion magnet supply, MRI/NMR, accelerators, and proton therapy. The claim is scoped honestly: the high field is a *system field* result, not a stand-alone-coil record; the small-bore plug coil is structurally infeasible as a bare winding but resolved by a stress-managed structural shield (feasible-pending-FEA); and the winding-tape experiment returned a *null result*. The value is the method, not a field record.

THE TEAM

Founding partners, board, advisors & auditors

Kronos is built by a bench of advanced-fuel-fusion, high-field-magnet, direct-conversion, and materials specialists, with a board and operations team drawn from defense, national laboratories, and industry. Dates are shown as ranges; where a tenure has ended or is term-ending, the range says so.

FOUNDING PARTNERS — SCIENCE

Dr. Gerald Kulcinski
Co-Founder · Helium-3 & Advanced-Fuel Fusion
UW–Madison · 2023–Present

Dr. Carl Weggel
Chief Scientist / S.M.A.R.T. Design
MIT Alcator Program · 2022–Present

Dr. Robert J. Weggel
Magnetic Field Design
MIT Magnet Lab · 2022–Present

BOARD

Priyanca Ford
Founder & CEO · Executive Board
2022–Present

Bandel Carano
Finance / Strategy
Oak Investment Partners / Stanford · 2025–2026

Patrick Schweiger
Fusion Device Engineering
Oklo / CFS / TerraPower · 2025–Present

SCIENTIFIC ADVISORS

Dr. Steven O. Dean
Fusion Policy & History
DOE / Fusion Power Associates · 2025–Present

Dr. Patrick H. Diamond
Plasma Turbulence & Transport
UC San Diego · 2025–Present

Dr. Jack J. Dongarra
HPC & Numerical Algorithms
Turing Award · 2025–Present

Dr. Nasr M. Ghoniem
Chief Material Scientist
UCLA · 2025–Present

Dr. Siegfried Glenzer
Plasma Physics & Laser Fusion
Stanford / SLAC · 2022–Present

Dr. David A. Hammer
Pulsed-Power Fusion
Cornell · 2025–Present

Dr. Donald A. Spong
Plasma Theory & Confinement
ORNL · 2025–Present

Dr. Curtis Smith
Risk Assessment & Nuclear PRA
MIT / Idaho National Lab · 2025–Present

RADM (Ret.) David Goggins
Naval Engineering & Power-Plant Design
U.S. Navy · 2023–2026

Dr. Konstantin Batygin
Mathematician
Caltech · 2022–2025

Dr. Ruben Fair
Magnet Design / ITER Liaison
PPPL / Jefferson Lab · 2022–2025

Dr. Paul S. Weiss
Materials & Nanotechnology
UCLA · 2022–2025

SCIENTIFIC AUDITORS

Dr. Wilfred A. Cooper
Plasma Equilibrium Theory
EPFL / Swiss Plasma Center · 2025–Present

Dr. Ahmed Hassanein
Plasma–Material Interactions
Purdue / Argonne · 2025–Present

Dr. Patrick E. Hopkins
Extreme Thermal Materials
U. of Virginia · 2025–Present

Dr. Peter Hosemann
Materials Joining & Structural Integrity
UC Berkeley · 2025–Present

Dr. Travis W. Knight
Advanced Nuclear Fuels & Systems
U. of South Carolina · 2025–Present

Dr. Philippe Lebrun
Cryogenics & Magnet Cooling
CERN · 2025–Present

Dr. Nitendra Singh
Nuclear Safety & Fuel Cycle
ITER · 2025–Present

Dr. Guido Van Oost
Magnetic Confinement & Fusion Systems
Ghent University · 2025–Present

Dr. Gary S. Was
Radiation Materials & Structural Integrity
U. of Michigan · 2025–Present

Dr. Ray Sedwick
Direct Energy Conversion
U. of Maryland · 2025

OPERATIONS

Michael Laughlin
Chief Operating Officer
2022–Present

Martin Owens
Chief Strategy Officer
LANL / GE Hitachi · 2022–Present

MG (Ret.) Paul Pardew
Chief Contracting Officer
Army Contracting Command · 2022–Present

David Beck
Fusion Commercialization
U.S. Space Force · 2024–Present

Sushma Bhatia
Environmental & Legislative
Google · 2022–Present

Michael De Frenza
Technology Licensing
2023–Present

MG (Ret.) Robin L. Fontes
Cybersecurity & Defense
Army Cyber Command · 2022–Present

Vijay Gehani
Supply Chain & Components
INOX India · 2024–Present

Jon Michel Greenwood
IT & AI Infrastructure
Live Nation · 2023–Present

Brian C. O'Neill
National Security
CIA / ODNI · 2022–Present

Gen. (Ret.) Gustave F. Perna
DoD Liaison
Operation Warp Speed · 2022–2023

Andrea Romero
Marketing Lead
2022–Present

Legal counsel is retained; those roles are held on the internal roster and are not listed here.

SOURCES

References

1 A Bondeson and D J Ward, Stabilization of external modes in tokamaks by resistive walls and plasma rotation, *Phys. Rev. Lett.* **72** 2709 (1994). doi:10.1103/PhysRevLett.72.2709

2 M S Chu and M Okabayashi, Stabilization of the external kink and the resistive wall mode, *Plasma Phys. Control. Fusion* **52** 123001 (2010).

3 H Biglari, P H Diamond and P W Terry, Influence of sheared poloidal rotation on edge turbulence, *Phys. Fluids B* **2** 1 (1990). doi:10.1063/1.859529

4 T S Hahm and K H Burrell, Flow shear induced fluctuation suppression in finite aspect ratio shaped tokamak plasma, *Phys. Plasmas* **2** 1648 (1995). doi:10.1063/1.871313

5 K H Burrell, Effects of $\boldsymbol{E} \times \boldsymbol{B}$ velocity shear and magnetic shear on turbulence and transport in magnetic confinement devices, *Phys. Plasmas* **4** 1499 (1997). doi:10.1063/1.872270

6 R E Waltz, G D Kerbel and J Milovich, Toroidal gyro-Landau fluid model turbulence simulations in a nonlinear ballooning mode representation with radial modes, *Phys. Plasmas* **1** 2229 (1994).

7 R Fitzpatrick, Bifurcated states of a rotating tokamak plasma in the presence of a static error-field, *Phys. Plasmas* **5** 3325 (1998). doi:10.1063/1.873000

8 R J Buttery *et al*, Error field mode studies on JET, COMPASS-D and DIII-D, and implications for ITER, *Nucl. Fusion* **39** 1827 (1999). doi:10.1088/0029-5515/39/11Y/323

9 R J La Haye, Neoclassical tearing modes and their control, *Phys. Plasmas* **13** 055501 (2006). doi:10.1063/1.2180747

10 J E Rice *et al*, Inter-machine comparison of intrinsic toroidal rotation in tokamaks, *Nucl. Fusion* **47** 1618 (2007). doi:10.1088/0029-5515/47/11/025

11 O Sauter, C Angioni and Y R Lin-Liu, Neoclassical conductivity and bootstrap current formulas for general axisymmetric equilibria and arbitrary collisionality regime, *Phys. Plasmas* **6** 2834 (1999). doi:10.1063/1.873240

12 E A Belli and J Candy, Kinetic calculation of neoclassical transport including self-consistent electron and impurity dynamics, *Plasma Phys. Control. Fusion* **50** 095010 (2008). doi:10.1088/0741-3335/50/9/095010

13 E A Belli and J Candy, Full linearized Fokker–Planck collisions in neoclassical transport calculations, *Plasma Phys. Control. Fusion* **54** 015015 (2012).

14 J W Connor, R J Hastie and J B Taylor, Shear, periodicity, and plasma ballooning modes, *Phys. Rev. Lett.* **40** 396 (1978). doi:10.1103/PhysRevLett.40.396

15 T C Hender *et al*, Progress in the ITER Physics Basis Chapter 3: MHD stability, operational limits and disruptions, *Nucl. Fusion* **47** S128 (2007).

16 F Troyon *et al*, MHD-limits to plasma confinement, *Plasma Phys. Control. Fusion* **26** 209 (1984). doi:10.1088/0741-3335/26/1A/319

17 J Candy and R E Waltz, An Eulerian gyrokinetic-Maxwell solver, *J. Comput. Phys.* **186** 545 (2003). doi:10.1016/S0021-9991(03)00079-2

18 J Candy, E A Belli and R V Bravenec, A high-accuracy Eulerian gyrokinetic solver for collisional plasmas, *J. Comput. Phys.* **324** 73 (2016). doi:10.1016/j.jcp.2016.07.039

19 F Jenko, W Dorland, M Kotschenreuther and B N Rogers, Electron temperature gradient driven turbulence, *Phys. Plasmas* **7** 1904 (2000). doi:10.1063/1.874014

20 C R Sovinec *et al*, Nonlinear magnetohydrodynamics simulation using high-order finite elements, *J. Comput. Phys.* **195** 355 (2004). doi:10.1016/j.jcp.2003.10.004

21 B Dudson *et al*, FreeGS: free-boundary Grad–Shafranov equilibrium solver (2020). doi:10.5281/zenodo.3745669

22 N C Amorisco *et al*, FreeGSNKE: a Python-based dynamic free-boundary toroidal plasma equilibrium solver, *Phys. Plasmas* **31** 042517 (2024). doi:10.1063/5.0188467

COLOPHON

How this document was made

The Kronos Fleet — Combined Editorial, 2026 is set in **Fraunces** (display), **Gelasio** (text), and **IBM Plex Mono** (data & equations), carried forward from the Kronos editorial design system.

The figures are rendered at 300 dpi from the deposited generator scripts; the document is composed as a single self-contained file with embedded fonts and imagery, paginated to US Letter, and rendered to PDF through a headless Chromium engine in matched light and dark editions.

Every headline quantity carries an evidence class; withdrawn and restated values are marked as such. Nothing herein is frozen beyond the founder-approved Tier-A set.

Explore it live — turn the interactive 3-D model, run the deposited solvers in the physics validator, and watch the companion film series.

LEGAL NOTICE

Notice, status, and distribution

Conceptual design & simulation study. This document reports a conceptual design and simulation study. It is not a construction commitment, a safety-analysis report, a regulatory filing, or an offer of securities. Forward-looking statements — schedules, costs, market sizes, and performance — are estimates subject to the limitations set out in the Simulations part and may change.

Numbers and their classes. Quantities are reported with evidence classes and case labels; modelled, assumed, and requirement-class values are identified as such and are not to be quoted without their labels.

Public edition. This edition carries the physics and design only; all financial, funding, and defense-commercial content has been removed for public distribution. The scientific text corresponds to the arXiv and journal submissions.

THE 2026 KRONOS SERIES

One programme, many papers

This editorial is one paper in the Kronos 2026 series — a real fusion company's complete, reproducible physics record for a spherical-tokamak breeder and its low-neutron D–^{3}He tandem-mirror burners. Every headline number is a frozen anchor in the Physics De-Risking Register.

Explore the whole programme: the De-Risking Register, the interactive 3-D model, and the physics validator.

KRONOS FUSION ENERGY

Toroidal Rotation, Flow-Shear Stabilization and Error-Field Correction in a Compact Spherical-Tokamak Breeder: Residual Transport and Locked-Mode Avoidance

A real fusion company building real machines. Explore the science, live.

Zenodo · doi:10.5281/zenodo.22645907

Read on kronosfusionenergy.com

The Physics De-Risking Register